ISOLATION OF AMBIENT AEROSOLS OF KNOWN CRITICAL SUPERSATURATION: THE DIFFERENTIAL CRITICAL SUPERSATURATION SEPARATOR (DS_CS)

A Thesis

by

ROBERT JOHN OSBORN

Submitted to the Office of Graduate Studies of
Texas A&M University
in partial fulfillment of the requirements for the degree of

MASTER OF SCIENCE

May 2007

Major Subject: Atmospheric Sciences

ISOLATION OF AMBIENT AEROSOLS OF KNOWN CRITICAL SUPERSATURATION: THE DIFFERENTIAL CRITICAL SUPERSATURATION SEPARATOR (DS_CS)

A Thesis

by

ROBERT JOHN OSBORN

Submitted to the Office of Graduate Studies of
Texas A&M University
in partial fulfillment of the requirements for the degree of

MASTER OF SCIENCE

Approved by:

Chair of Committee,	Don R. Collins
Committee Members,	Sarah D. Brooks
	Simon W. North
Head of Department,	Richard E. Orville

May 2007

Major Subject: Atmospheric Sciences

ABSTRACT

Isolation of Ambient Aerosols of Known Critical Supersaturation:

The Differential Critical Supersaturation Separator (DS_cS). (May 2007)

Robert John Osborn, B.S., Texas A&M University

Chair of Advisory Committee: Dr. Don Collins

A field-deployable instrument has been developed that isolates from an ambient aerosol population only those particles that have critical supersaturations, S_c, within a narrow, user-specified, range. This Differential Critical Supersaturation Separator (DS_cS) is designed to supply one or more particle size and/or composition analyzers to permit the direct examination of the factors that influence the activation properties of ambient aerosols. The DS_cS consists of two coupled parallel plate continuous flow thermal gradient diffusion cloud chambers housed within a single enclosure. Descriptions of instrument operation, construction and calibration data collected, when pure ammonium sulfate aerosols were injected into the DS_cS for operation at $0.15\% < S_c < 0.175\%$, $0.30\% < S_c < 0.35\%$, and $0.60\% < S_c < 0.70\%$, are included. Following instrument development, the DS_cS was deployed during March 2006 for the Megacities Impact on Regional And Global Environment (MIRAGE) field campaign in Mexico City, Mexico. Throughout the MIRAGE field campaign a Differential Mobility Analyzer/Tandem Differential Mobility Analyzer (DMA/TDMA) system measured aerosol size distributions and size-resolved hygroscopicity of DS_cS separated aerosol. The dry diameter (D_p*) of particles sampled in the TDMA system as well as the known

S_c prescribed in the DS_cS were combined in a modified version of Köhler Theory to make predictions of particle hygroscopicity. These predictions frequently overestimated the measurements. Further analysis of DS_cS separated aerosols compares the known particle S_c to a predicted particle S_c, providing insight into particle activation efficiency. Overall, the sampled aerosol exhibited properties that indicate they were more efficient at activation than Köhler Theory would predict.

DEDICATION

This manuscript is dedicated to all of my family and friends who have supported me through the years.

ACKNOWLEDGMENTS

I would like to thank my advisor, Dr. Don Collins for guiding me and supporting my research with superb patience. I greatly appreciate everything he has done for me including giving me the opportunity to study in Mexico. Furthermore, I would like to express my thanks to my co-workers Runjun Li, Crystal Reed, Chance Spencer, Nathan Taylor and Jason Tomlinson, for their ideas and support throughout this work. I would also like to thank the members of my advisory committee, Dr. Sarah Brooks and Dr. Simon North, for taking time out of their busy schedules to assist in editing this manuscript. Last, but not least, I would like to thank my family and friends, especially my wife Kimberly, my mom, and my dad for all of the support they have given me throughout my graduate career.

This study was supported by The National Science Foundation Atmospheric Chemistry and Physical Meteorology programs through grant ATM-0094342.

TABLE OF CONTENTS

LIST OF FIGURES

1. INTRODUCTION

The role of aerosols in cloud formation by serving as cloud condensation nuclei (CCN) has been known for over a century (Aitken, 1880a; 1880b). Understanding the droplet activation properties of aerosols is important due to the direct and indirect effects on climate. A higher concentration of cloud droplets in a given cloud has been shown to increase albedo (Ackerman et al., 2000; Twomey, 1977), increase cloud lifetime (Charlson et al., 1992), and decrease precipitation efficiency (Rosenfeld, 1999), resulting in a net cooling effect on the global scale. The preferential growth of CCN through cloud processing also impacts the size-dependent addition of mass to an aerosol population. This may enhance its scattering efficiency, and consequently, its single scattering albedo (Hegg et al., 2004). Conversely, the preferential removal of larger and generally less light absorbing CCN during precipitation events may result in the reduction in single scattering albedo. To characterize the aforementioned effects of CCN on climate, scientists strive to better understand the link between the measurable properties of aerosol particles and their activation into cloud droplets under prescribed conditions.

An aerosol will activate only if the water vapor supersaturation (S) surrounding the particle exceeds its critical supersaturation (S_c). Once this occurs, water vapor

---

This thesis follows the style of *Aerosol Science and Technology*.

rapidly condenses on the droplet, and typically continues doing so until its surroundings become subsaturated. As a result, when air becomes supersaturated, all particles with S_c values below or equal to the ambient supersaturation will activate, yielding some concentration of cloud droplets. The factors controlling S_c include chemical composition, size, shape, surface tension, and temperature of the aerosol. Improvement in the accuracy of the predictions of the indirect effect of aerosols on climate relies on the inclusion of this information in any numerical model that calculates CCN spectra. For ease of calculation, current climate models use parameterized empirical functions to retrieve a CCN spectrum (Jones et al., 2001; Penner et al., 2001). These empirical functions incorporate limited information of the controlling factors, which introduces error. Other models, such as global aerosol models, include more details of activation efficiency which results in better predictions of CCN spectra (Spracklen et al., 2005; Adams and Seinfeld, 2003; 2002; Gong et al., 1997). However, even the most accurate model predictions today are limited by poorly understood activation efficiencies of complex mixtures representative of ambient aerosols.

Laboratory studies have been implemented to increase understanding of ambient aerosol activation efficiency for more accurate model parameterizations. Such studies often focus on quantifying the activation properties of laboratory-generated particles. Extrapolation of the results of these studies that often employ relatively simple particles to describe the behavior of multicomponent ambient aerosols is challenging. Recent studies indicate that different organics and organic-mixtures have vastly different activation properties (Henning et al., 2005; VanReken et al., 2005). VanReken et al.

(2005) studied activation efficiency of biogenic secondary organic aerosols (SOA). Results from that study suggest that SOA formed from organic precursor gases of similar molecular weight possess different activation properties that vary with age of the aerosol. Other work has shown complex mixtures of inorganics and organics have diverse activation properties (Bilde and Svenningsson, 2004).

Closure studies are designed to test the accuracy with which CCN concentrations can be predicted from ambient aerosol size distributions and size resolved chemical composition. In a closure study, measurements of activated CCN concentrations at given supersaturations are compared to concentrations of activated CCN predicted when measured ambient aerosol chemical and physical properties are used in Köhler Theory. Closure is said to be achieved when predictions match observations. Achievement of closure provides confidence in the techniques used to apply results from laboratory or theoretical studies to the ambient environment; lack of closure may provide insight into remaining sources of uncertainty. A more recent closure study by Cantrell et al. (2001) attempted CCN closure during the Indian Ocean Experiment (INDOEX) and was successful over a wide range of supersaturations in 8 out of 10 cases. The two unsuccessful cases occurred when the aerosol had been influenced anthropogenically, in which the predicted CCN concentration exceeded that measured. (VanReken et al., 2003) achieved CCN closure at 0.20% and 0.85% supersaturations during the CRYSTAL-FACE campaign. Chuang et al. (2000) attempted closure during the second Aerosol Characterization Experiment (ACE-2) at 0.1% supersaturation without success perhaps as a result of instrumentation error and/or limited knowledge of certain CCN

activation efficiencies. Additional closure studies have aimed to predict CCN concentrations from measured aerosol size distributions and size-resolved hygroscopicity (Covert et al., 1998; Gasparini et al., 2006), Summarizing results of all studies of this type is complicated by variability in both the instruments used to measure CCN concentrations and those used to characterize the aerosol. Instruments such as the Droplet Measurement Technologies CCN counter (Roberts and Nenes, 2005), the cloud condensation nuclei Remover (CCNR; Ji et al., 1998), the isothermal haze chamber (Alofs, 1978), and the static diffusion cloud chamber (Sinnarwalla and Alofs, 1973; Twomey, 1963) utilize different CCN detection techniques and have all been used in CCN closure studies. Additionally, different investigators use different algorithms and assumptions to relate the characterized aerosol to CCN concentrations.

A more direct and meaningful evaluation of the link between S_c and measurable aerosol properties is possible if the previously activated aerosol is first isolated in a manner that preserves particulate mass and composition. Alofs et al. (1997) developed a system combining activation chambers and virtual impactors designed to collect milligram quantities of CCN. In this system, CCN that activate at different prescribed supersaturations are isolated and collect on filters for chemical analysis. Since the aerosol is not dried, it is difficult to determine the size range of particles that activated at a certain supersaturation. Additionally, sample durations as long as a day are required to collect sufficient aerosol mass, during which the ambient aerosol characteristics will likely vary. Perhaps the most widely used instrument capable of separating CCN from ambient aerosols is the Counterflow Virtual Impactor (CVI) which is designed to isolate

larger cloud droplets in a sample flow without contamination of smaller unactivated particles (Noone et al., 1988; Ogren et al., 1985). Although it is desirable to quantify CCN concentration at the local in-cloud supersaturation for certain analyses, the imprecise knowledge of that supersaturation limits the utility of the data for refining cloud-aerosol linkages in models in which supersaturation is prescribed. Additionally, Operation of the CVI in a traditional manner limits the use to within cloud, therefore, it is typically used on an airplane or on top of a mountain, potentially raising operation costs. (Sorooshian et al., 2006; Glantz et al., 2003; Twohy et al., 2001; Wobrock et al., 2001) Supersaturation dependent CCN concentration and/or properties could be quantified by operating a CVI downstream of a inlet in which a prescribed supersaturation is maintained. Harrison and Harrison (1985) describes a high-flux thermal diffusion cloud chamber designed for this type of analysis albeit with a virtual impactor rather than a CVI, which results in some contamination of the separated flow by smaller, unactivated, particles. However, because the sampled aerosols are not confined in the cloud chamber, particles along different streamlines are exposed to different supersaturations limiting any detailed quantitative analysis of particle activation.

The constraints realized in the above instrumentation have inspired the design of a new instrument called the Differential Critical Supersaturation Separator (DS_cS), which is capable of retrieving the population of particles that activate when exposed to a controlled, narrow, user-specified supersaturation range. This separated aerosol remains suspended, thereby enabling subsequent analysis using a variety of instruments

downstream. In house calibration of the DS_cS was performed to ensure proper operation and is presented in the following work. Additionally, the DS_cS was recently deployed for the Megacities Impact on Regional And Global Environment (MIRAGE) field campaign in Mexico City, Mexico. A discussion of data collected throughout this project is presented as well.

2. INSTRUMENT DESCRIPTION

2.1 Instrument Operation

The DS_cS is a combination of two parallel plate continuous flow thermal gradient diffusion chambers in series. The first diffusion chamber, called the CCN Remover (CCNR), is a modification of the CCNR developed by Ji et al. (1998). This chamber serves as a high pass filter for aerosol based on critical supersaturation. The second diffusion chamber, the CCN Separator (CCNS), has a similar design to the CCNR yet incorporates ideas from Sun and Reiss (1984) which facilitate the bifurcation of aerosols based on critical supersaturation. Figure 1 illustrates the side profile of the DS_cS with the locations of the two activation chambers indicated.

The CCNR contains two wetted surfaces consisting of an upper saturated piece of filter paper 1.9 cm above a lower exposed freshwater bath. A linear temperature and vapor pressure gradient is established in this chamber by controlling the filter paper and the lower bath temperatures. The bottom bath is always held cooler than the filter paper above to prevent convectional mixing in the chamber. Profiles of temperature and vapor pressure established in the chamber are used together with the Clausius-Clapeyron equation to derive the supersaturation profile (Figure 2). Sample aerosols, sandwiched between two layers of particle-free sheath flow, are injected into the layer of peak supersaturation (S_p) from the initial inlet ramp. Particle-free sheath flow is introduced at both edges of the aerosol sample flow, extending inward from the sides of the chamber, diminishing any unwanted edge effects. Once exposed to the maximum CCNR

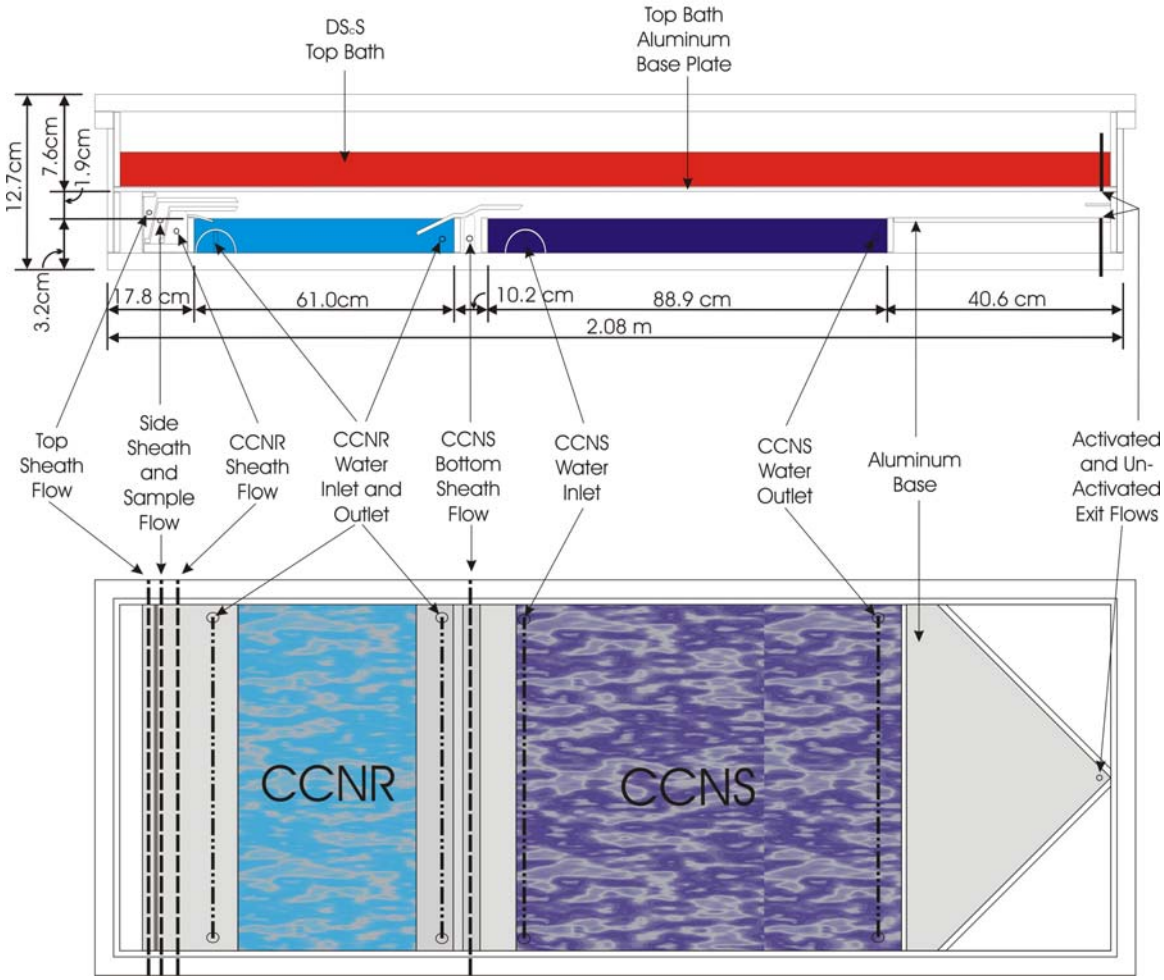

Figure 1. Side profile and top view of the DS_cS. Locations of both activation chambers, air and water inlet tubes are labeled. Colors represent different bath temperatures ranging from the warmest (red) to the coldest (dark blue).

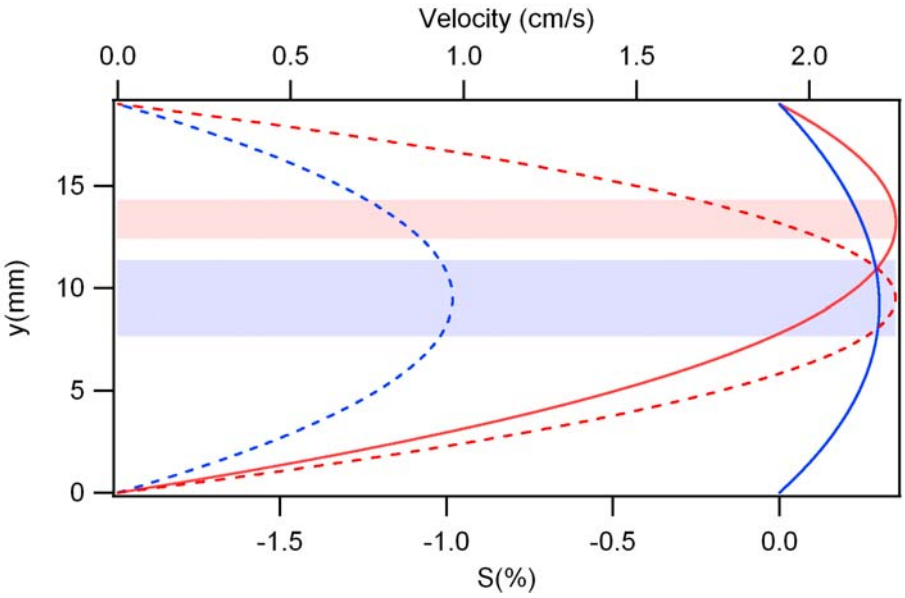

Figure 2. Simulated Velocity profiles, S profiles (dashed and solid lines respectively), and sample aerosol layer injection positions (shaded regions) in the CCNR (blue) and the CCNS (red) chambers calculated for a S_c range of 0.3%-0.35%.

supersaturation, activated aerosols gain sufficient mass and gravitationally settle out of the sample layer into the bath below while the

Sun and Reiss (1984) developed a static thermal diffusion cloud chamber that utilizes an acidic solution to generate a subsaturated region beneath a supersaturated region for the purpose of activating and evaporating aerosols. The CCNS adapts this idea in a continuous flow orientation similar to the CCNR by replacing the lower freshwater bath with a saline solution that produces the same subsaturating effect. As in the CCNR, the lower bath in this section is maintained at colder temperatures than the saturated filter paper above. To derive the supersaturation profile in the CCNS (Figure 2), the empirical relationship developed by Tang and Munkelwitz (1994) is first used to describe the vapor pressure at the surface of the saline solution followed by the same calculation procedure used for the CCNR. Sodium sulfate, a less corrosive salt, is dissolved in the bath for supersaturations up to 0.4%. At higher supersaturations the amount of dissolved salt increases and solution temperature decreases, leading to the transformation of sodium sulfate into a solid decahydrate known as glauber's salt. Sodium chloride replaces sodium sulfate as the dissolved salt in these conditions. The layer of subsaturation created by the solution elevates the layer of maximum supersaturation relative to the CCNR. The introduction of additional sheath flow beneath the total CCNR flow elevates the sample aerosol into the layer of maximum supersaturation within the CCNS and increases flow velocity in the chamber. A secondary ramp separates the CCNR flow from the added sheath flow for 12.7 cm, abating any incidental mixing between the two flows. To maintain a comparable

residence time of particles in both chambers, the length of the CCNS is almost twice as long as the CCNR. Upon activation, cloud drops fall due to gravitational settling into the layer of subsaturation and evaporate, forming a second layer of aerosol. To retrieve CCN activated between a narrow supersaturation range, the maximum supersaturation prescribed in the CCNR is maintained just below the maximum supersaturation value prescribed in the CCNS. If the maximum value in the CCNR is above the maximum value in the CCNS, no particles will be separated since all particles with a critical supersaturation equal to CCNS maximum supersaturation are lost in the CCNR.

Following the CCNS chamber all flow enters the DS_cS exit region. Vertical acrylic walls in this section converge the total flow in the chamber to the vertical midpoint at the end of the chamber. Aerosols that did not activate (unactivated aerosol) are extracted from the top of the chamber and aerosols that did activate (activated aerosol) are extracted from the bottom of the chamber. Both flows are subsequently dried and made available for analysis downstream.

2.2 DS_cS Chamber Construction

Dimensions of the DS_cS were chosen to obtain the highest flow rates possible for increased measurement statistics, with ease of movement in consideration. The DS_cS rests atop a 2.13 m X 0.86 m X 1.39 m aluminum frame containing all of the external parts needed for operation. A 1.27 cm thick piece of acrylic rests on top of the aluminum frame providing extra insulation for the base of the instrument and a surface to mount 35-4.92 cm tall X 10.16 cm O.D. X 1.27 cm thick cylindrical supports to. The

exterior shell of the DS_cS rests on these supports and consists of a 2.08 m X 76.2 cm X 11.4 cm box constructed of 1.27 cm thick acrylic with a 3.81 cm wide lip cemented to the top. A 1.27cm thick acrylic lid clamps to the lip and with the aid of a continuous 2.54 cm wide X 0.64 cm thick neoprene foam rubber gasket creates a leak-free seal. Surrounding the interior vertical wall of the DS_cS is an interior frame made from 4.45 cm tall strips of 1.27cm thick acrylic. Contained within this 'lower' frame are the entrance region, both activation chambers, and the exit region of the instrument. Dimensions in this section describe length in the chamber unless otherwise specified. The first 15.24cm of the lower section contains the flow entrance region where the aerosols are introduced into the CCNR portion of the chamber (Figure 1). Located 15.24 cm from the beginning of this section is the beginning of the initial flow inlet ramp used to position the sample aerosol layer in the center of the CCNR chamber. The 18.41 cm long X 71.12 cm wide X 4.45 cm tall ramp is constructed out of 0.32 cm and 0.64 cm thick 6065 alloy aluminum. The length of the ramp provides sufficient time for moderate flow disturbances that may develop to dissipate. Sheath flow air Inlet tubes, inserted through the inlet ramp, extend widthwise penetrating the exterior walls of the DS_cS. Inlet slits, .2032cm wide, extend lengthwise within the middle 71.12 cm of the 0.64 cm diameter sheath flow inlet tubes (in 8.61 cm long intervals with .32 cm gaps between 8 separate slits). A combination of an interior 0.64 cm diameter inlet tube with 0.20 cm inlet slits and an exterior 0.95 cm diameter inlet tube that has .51 cm thick inlet slits, with the exception of 0.02 cm thick slits cut at the outer edges, form the aerosol sample inlet tube (Figure 3). O-rings fitted between both tubes isolate an edge

sheath flow from the aerosol sample flow in the inlet tube. Filtered sheath air flows between the interior and exterior tube and all aerosol sample flow is introduced inside the interior tube. The locations of the inlet tubes in the chamber relative to the inlet ramp isolate each flow until ramp termination (Figure 1). Sheath flows in the top and bottom sections of this inlet flow through a sheet of photo-chemically etched stainless steel (BE 0805 MicroEtch Stainless Steel Screen; InterNet Inc., Anoka, MN) to further aid in flow disturbance dissipation.

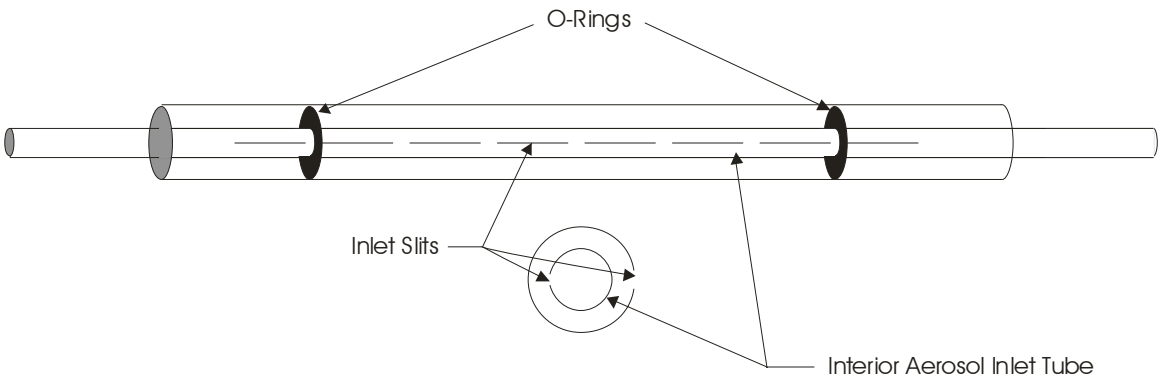

Figure 3. Sample inlet tube with O-Ring placement and slit pattern.

Following the entrance region lays a 2.54 cm tall X 1.27 cm thick strip of acrylic extending the width of the chamber creating a water barrier for the adjacent 0.51 m long CCNR freshwater bath. A plastic water injection tube with evenly spaced inlet holes follows the barrier. An acrylic tube, split in half lengthwise, with inlet slits cut in the side covers this inlet tube for added water flow dispersion. An identical plastic tube at the other end of the bath evenly pulls water from the bath. A second acrylic water barrier downstream contains the bath in the CCNR activation chamber region. Attached to the top of the downstream barrier is a secondary 23.8 cm long aluminum ramp used to squeeze the CCNR flow into the upper portion of the CCNS. For smooth flow transition into the next chamber, the second ramp bends into the CCNR freshwater bath for 7.62 cm (from the upstream barrier face). The CCNR flow is displaced 0.95 cm above the saltwater surface in the CCNS before the termination of the second ramp. An additional sheath flow inlet tube is positioned between a 7.62 cm long gap beneath the second flow ramp and encompassed by a layer of photo-chemically etched stainless steel (BE 0805 MicroEtch Stainless Steel Screen; InterNet Inc., Anoka, MN) stainless steel. A third acrylic water barrier adjacent to a 0.89 m long saltwater bath follows this gap. Water inlet and extraction tubes as described above are contained within this bath. A final acrylic water barrier resides at the termination end of the saltwater bath and supports the aluminum base plate of the exit region (Figure 1). Acrylic walls on both sides of the exit region converge flow to the center point of the chamber and support the previously mentioned aluminum base throughout the region. A stainless steel plate located at the vertical midpoint of this region extending 5.08 cm upstream from the chamber

termination point minimizes any mixing between the flows being extracted. A hole drilled through the bottom of the exit region plate 2.54 cm upstream from the chamber termination point and through the bottom of the acrylic below supports a stainless steel flow extraction tube. Immediately above this tube is a second hole that penetrates through the aluminum base of the top freshwater bath and supports an additional stainless steel flow extraction tube. The aluminum base of the top bath rests on top of the lower frame and provides the top surface for the activation chambers, and the entrance and exit regions. The perimeter of the top bath consists of 5.08cm tall strips of acrylic. To prevent deflection of the bottom aluminum plate into the activation chamber, 4 - 11.43 cm X 3.81 cm X 71.12 cm aluminum bars spaced widthwise through the bath are attached to the aluminum base. Channels cut perpendicularly through the bottom of the attached bars allow water to flow freely through the bath while maximizing water contact with the base. An acrylic barrier, also oriented widthwise, serves as a spillway that evenly distributes freshly injected water in this bath before flowing above both activation chambers. Several evenly spaced, vertically oriented, capillary tubes extend through the aluminum base plate, flush with the bottom, and are used in soak cycles as described in the water flow section. An air void between the surface of the top bath and the DS_cS lid allows room for varying bath heights during soak cycles. Eight evenly spaced 4.45 cm tall strips of acrylic cemented widthwise to the lid and base (four each) of the DS_cS provide extra support needed to resist deflection induced by a vacuum produced when operating instrument. An exterior insulation box made from 1.27 cm thick acrylic encases the DS_cS during operation.

2.3 Water Flow

The success of the DS_cS partially depends on its ability to control temperatures of the water baths over long periods of time. A system of thermometers, water pumps and water chillers are used to maintain constant temperatures throughout operation. Combinations of Tygon and stainless steel tubing form the DS_cS waterlines. Three centrifugal aquarium pumps circulate through all three baths (Little Giant Pump Co. Oklahoma City, OK). One VWR model 1197P chiller (cold chiller) and one VWR model 1187P chiller (warm chiller) control the temperature of the water in all baths with help from PID controls in the operation software. Two separate pumps, located inside the chillers, circulate water around submerged coils. Water temperature in the top bath is measured with two 2.54 cm long YSI stainless steel encased thermocouples placed above the center of each activation chamber. Water turnover rates of twice per minute for the top and CCNS bath, as well as once per minute in the CCNR bath serve to reduce any temperature anomalies. Temperatures in the two bottom baths are also measured with YSI stainless steel encased thermocouples. One 2.54 cm long thermocouple at the center of each bath is oriented vertically to read the temperature just below the water surface and one 10.16cm long thermocouple penetrates the side of the chamber 1.27 cm below the surface of each bath.

Figure 4 illustrates the water flow path for the entire instrument with relative bath temperatures indicated. Flow for the CCNR bath follows a more elaborate path due to the intermediate temperature the bath is maintained at. Upon exiting the CCNR bath, water in flows through a pump leading to a tee. From here, water either travels to a coil

in the cold chiller or to a Teknocraft Inc. Solenoid Control Valve (SCV) followed by another coil submerged in the warm chiller. A computer controls the flow through the SCV to adjust the bottom CCNR bath temperature. Both water flows subsequently combine into one main line and pass through the flow conditioning tube, the purpose of which is described in the air flow section below, inside of a submerged 1.27 cm diameter stainless steel tube. Water then flows to the water injection tube inside the chamber, ending the CCNR water flow cycle. Saltwater in the CCNS bath follows a simpler path that first exits the bath, encounters a water pump, followed by a coil in the cold chiller and then re-enters the bath. The temperature of this bath is controlled by adjusting the temperature of the cold chiller. To ensure that water in the two bottom baths stays well mixed, minimizing any temperature or salinity gradients, eight submerged stirrer magnets are placed just above external magnets mounted on small fans beneath the exterior frame. Submerged pieces of filter paper rests atop a sheet of porous stainless steel just below the water surface in both bottom baths to attenuate disturbances from the mixers below.

Water Flow Schematic

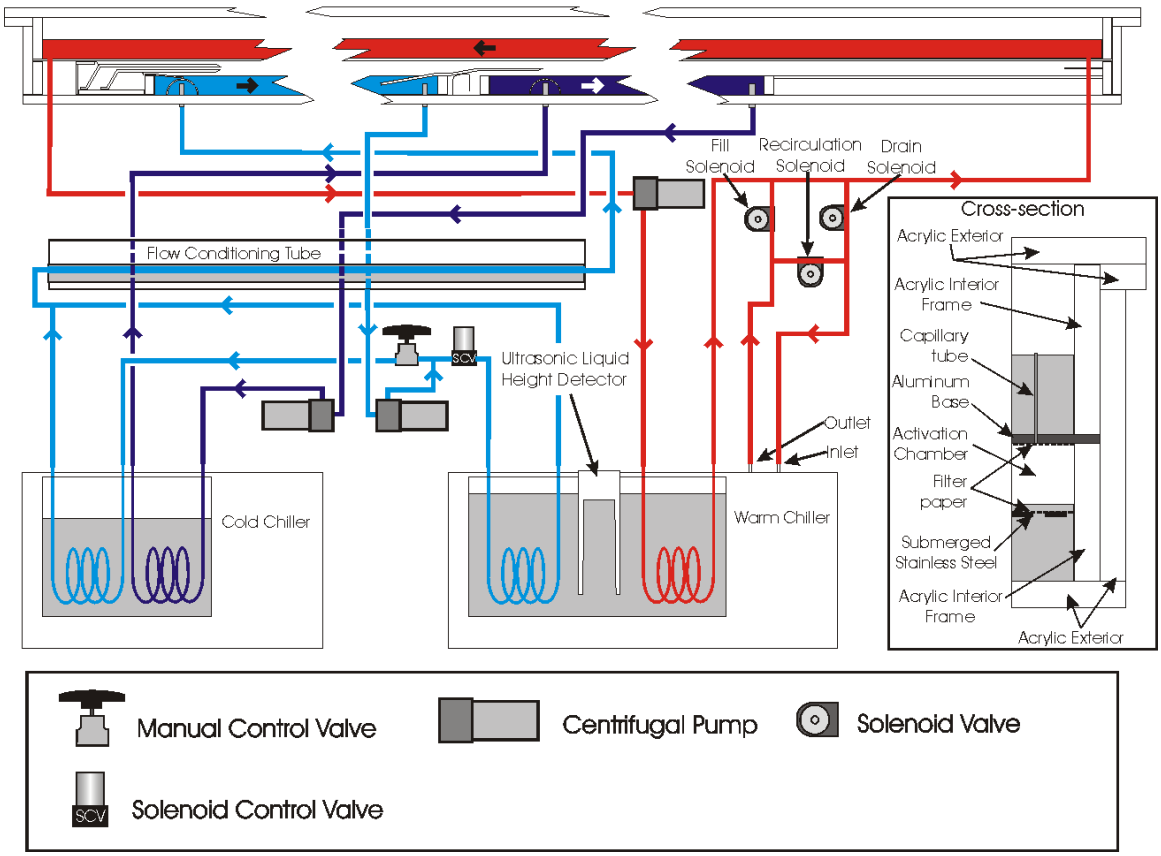

Figure 4. DS_cS water flow schematic. Water flow lines are color coded corresponding to their respective baths and arrows indicate flow direction. Grey shading represents additional locations of water in the system unless otherwise noted.

The top bath in the DS_cS extends the entire length of the instrument. This bath is removed during initial instrument setup and for instrument cleaning. The water in this bath follows a path that first exits the DS_cS, then enters the pump, flows through a coil in the warm chiller and is then pumped back into the bath. To reduce fluctuations of supersaturation caused by a slight relaxing of water temperature as a function of residence time in the chamber, the flow direction is counter to the flow direction of the bottom baths. During normal operation, the recirculation solenoid shown in Figure 4 is opened while the fill and drain solenoid are closed, isolating the water flow from the warm chiller. Over time, water vapor contained within the filter paper attached to the top bath aluminum base is depleted, after which it must be replenished. Periodically, a soak cycle is initiated, during which the fill solenoid is opened and the recirculation solenoid is closed (while the drain solenoid remains closed). This process allows water to fill the top bath eventually submerging the capillary tubes allowing water to drip into the filter paper below. An ultrasonic liquid level height detector continuously monitors the amount of water remaining in the warm chiller, eventually indicating when a pre-determined soaking set-point is reached. Once the level of water in the warm chiller surpasses this set-point, the fill solenoid closes and the drain solenoid opens allowing water to re-enter the warm chiller. Normal chamber operation resumes once the chiller is refilled. This process is repeated in pre-determined intervals that depend on the rate of vapor diffusion from the filter paper. The entire water system contains about 107 liters of water and constantly pumps about 56 liters. With this amount of water, temperatures take 2 to 3 hours from initial startup to stabilize at the desired set-points.

2.4 Air Flow

Controlling air flow inside the DS_cS is just as important as controlling water flow. Figure 5 illustrates all components of the air flow system with flow directions labeled. The majority of the flow in the DS_cS is particle-free sheath flow. All air flow lines shown are composed of stainless steel tubing unless noted otherwise. The supersaturation profile in both chambers is rapidly established with the help of pre-saturated sheath flows. Vacuum pump exhaust air that is forced through a bubbler, to saturate the flow at room temperature, followed by a 1.5 m long horizontal flow conditioning tube, described in the water flow section, used to keep the flow saturated while cooling it to a temperature close to the CCNR bath. Only the required flow in the system passes through the horizontal flow conditioning tube, excess flow is vented through a tee between both saturators. A 0.22 micrometer polypropylene particle filter (DCP02000T9 Calyx capsule; Osmonics Inc., Westborough, MA) is placed downstream of the flow conditioning tube before flow is split into five separate lines. Four flow lines lead to sheath flows inlets (labeled in Figure 5) while the remaining line leads to the purge flow for the sample flow humidifying nafion bundle. Each sheath flow inlet

contains a Teknocraft Inc. SCV followed by a flow meter (Alicat Scientific, Tucson, AZ) to measure and control flow rates after which the flow is split and injected into both sides of their respective inlet tubes. The aerosol sample line simply consists of a humidifying nafion bundle, a SCV, a flow meter and an inlet tube. In the exit region, two previously discussed flow extraction tubes pull flow from the chamber and lead to a drying nafion bundle (Perma Pure LLC, Toms River, NJ), a flow meter and a tee that splits flow for downstream instrument sampling. A secondary tee downstream connects the vacuum pump lines to the system. Two GAST model 75R647-V101-H301X vacuum pumps pull flow through the chamber and all drying nafion purge flows. Total flow rates entering and exiting the DS_cS are compared to determine if there are leaks in the system. The air void immediately above the top bath is continuously recircluated through a filtering system consisting of a regenerative blower upstream of a HEPA-filter (12144 HEPA capsule; Pall Gelman Laboratory, Ann Arbor, MI) connected to the chamber with nylon tubing. This process eliminates the possibility of residual particles in this void straying into the activation chamber.

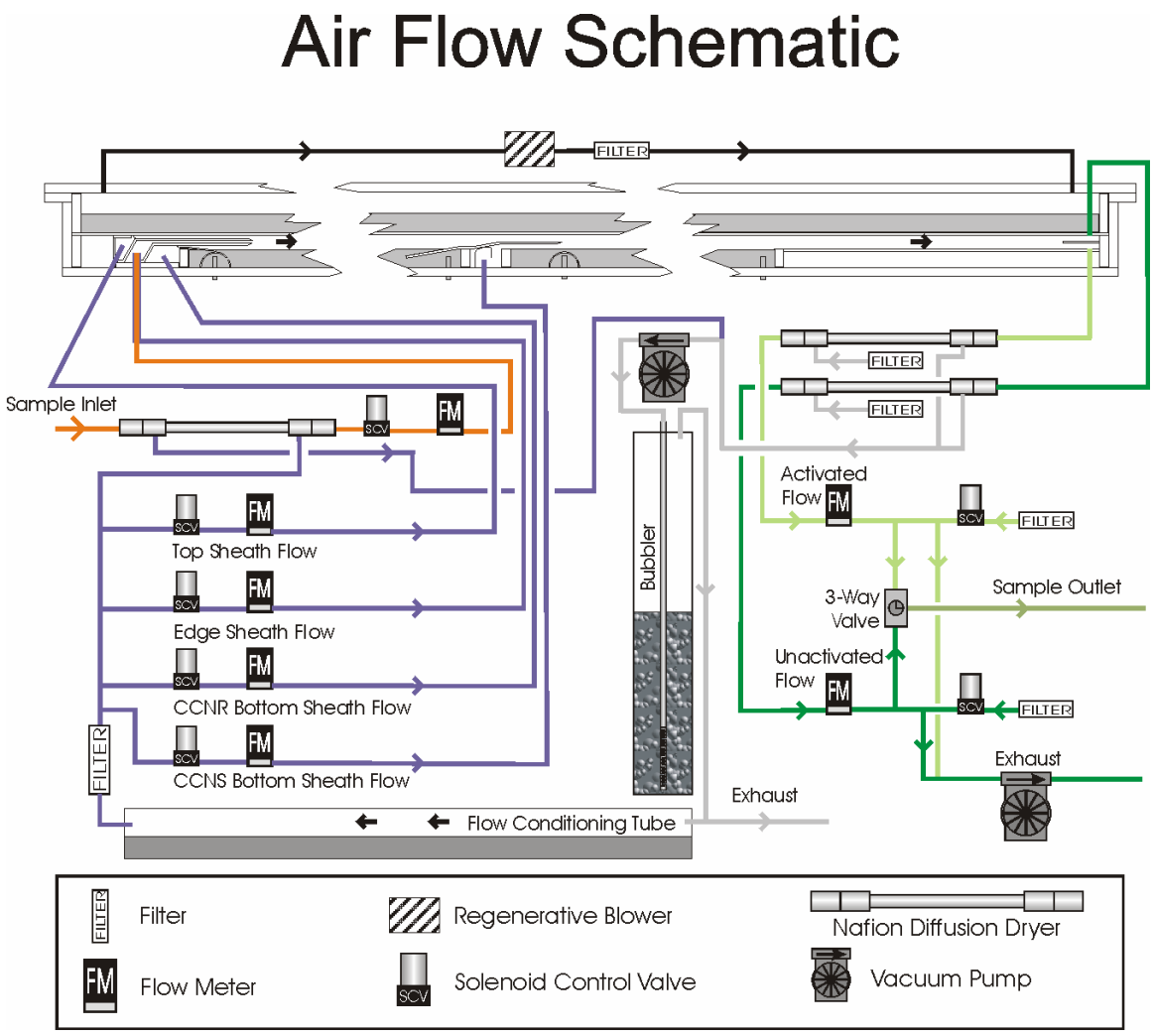

Figure 5. Air flow schematic with air flow direction in lines labeled with arrows.

A simple computer model that calculates cloud droplet growth is used to determine the flow rates used inside of the chamber. First, the time it takes for the cloud drop to fall the required deposition or evaporation distance is determined. The change in the diameter of an aerosol due to condensation of water vapor on its surface is calculated using the diffusional growth equation (Seinfeld and Pandis, 1998):

$$D_p \frac{dD_p}{dt} = \frac{S_{V,\infty} - \exp\left(\frac{4M_w\sigma_w}{RT_\infty\rho_w D_P} - \frac{6n_s M_w}{\pi\rho_w(D_P^3 - d_u^3)}\right)}{\frac{\rho_w RT_\infty}{4P^0(T_\infty)D_V^{'}M_w} + \frac{\Delta H_V\rho_w}{4K_a^{'}T_\infty}\left(\frac{\Delta H_V M_w}{T_\infty R} - 1\right)} \quad (1)$$

where D_p is the droplet diameter, $S_{V,\infty}$ is the ambient supersaturation, M_w is the molecular weight of water, σ_w is the surface tension of water, T_∞ is the ambient temperature, ρ_w is the density of water, n_s is the number of moles of solute, d_u is the diameter of the insoluble particle fraction, and ΔH_V is the enthalpy of evaporation for water. $D_V^{'}$ and $K_a^{'}$ are the modified diffusivity of water vapor in air and the modified thermal conductivity of air respectively (Fukuta and Walter, 1970; Pruppacher and Klett, 1978) and are represented as follows:

$$D_V^{'} = \frac{D_V}{1 + \frac{2D_V}{\alpha_c D_P}\left(\frac{2\pi M_w}{RT}\right)^{\frac{1}{2}}} \quad (2)$$

$$K_a^{'} = \frac{K_a}{1 + \frac{2K_a}{\alpha_T D_P \rho \hat{C}_P}\left(\frac{2\pi M_a}{RT_a}\right)^{\frac{1}{2}}} \quad (3)$$

Where α_c is water accommodation coefficient, α_T is the thermal accommodation coefficient, ρ is the density of air, $\hat{C}_P$ is the heat capacity of air at constant pressure, and M_a is the average molecular weight of air. The water accommodation coefficient (α_c) and the thermal accommodation coefficient (α_T) used are based on experimental data giving values of 0.05 and 1 respectively (Shaw and Lamb, 1999). The non-modified diffusivity of water vapor in air (D_V) and the non-modified thermal conductivity of air (K_a) are represented as:

$$D_V = \frac{0.211}{P}\left(\frac{T}{273}\right)^{1.94} \quad (4)$$

$$K_a = 10^{-3}(4.39 + 0.071T) \quad (5)$$

An initial particle diameter is determined before using equation (1) by calculating the critical diameter of a pre-specified aerosol type at a supersaturation adjusted below the actual maximum supersaturation in the each chamber. This ensures that the modeled aerosols are representative of an aerosol that is sure to activate and follow the calculated trajectory. Terminal velocity of the modeled droplet is simultaneously calculated with drop diameter:

$$v_t = \frac{1}{18}\frac{D_p^2 \rho_p g C_c}{\mu} \tag{6}$$

Where ρ_p is the particle density, C_c is the slip correction factor, and μ is viscosity. Iterations of equation (1) and (6) are taken at time steps that produce expected results. Equation (1) is calculated assuming pure ammonium sulfate aerosol.

Chamber air flow rates are computed once the time of droplet deposition is determined. Current operation utilizes 75% of the length of the chamber for droplet settling or evaporation to occur. Figure 6 shows calculated trajectories of CCN injected at the top, bottom and middle of the aerosol layer for various supersaturation ranges. Velocity profiles calculated for the S_c range of 0.3-0.35% are shown in Figure 2. It is important to note at lower supersaturations, flow rates must decrease considerably to account for increased droplet growth time, potentially degrading instrument performance.

Figure 7 illustrates the position of the flow cutoff line in the CCNS with respect to certain activated aerosol to unactivated aerosol flow ratios. The DS_cS is commonly set to extract 1/3 of the total flow from the activated aerosol outlet and 2/3 of the flow from the unactivated aerosol outlet. Based on model calculations, if the DS_cS were operated with a large enough unactivated to activated flow ratio, it would be possible to concentrate activated aerosols relative to their ambient concentrations. To do this, though, cloud drops must evaporate in a layer just above the surface of the saltwater where it is possible to reduce recovered aerosol concentrations due to particle deposition into the bath.

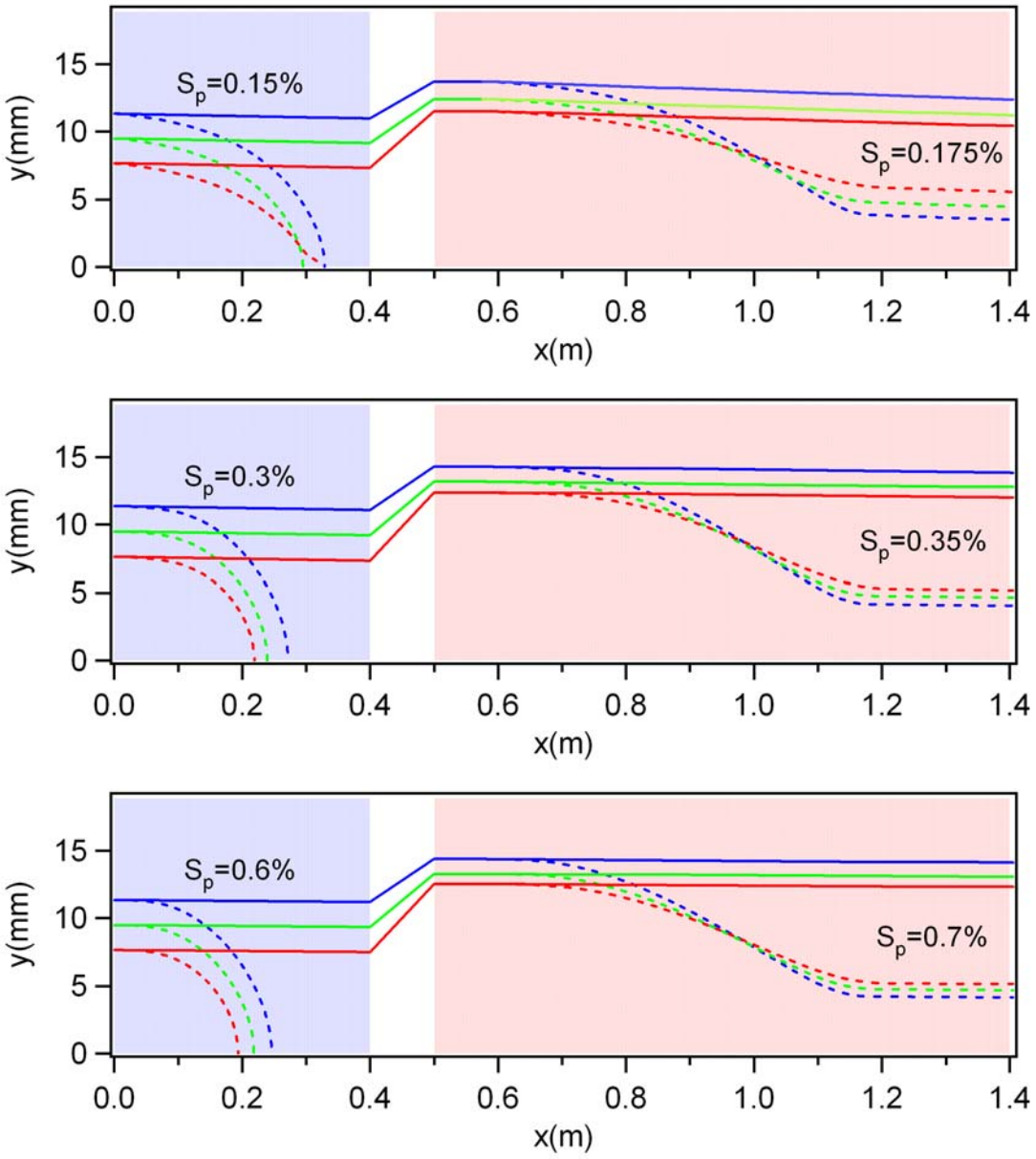

Figure 6. Simulated aerosol trajectories in both the CCNR and the CCNS with peak supersaturation values (S_p) labeled. The blue and red lines represent the upper and lower boundaries of the aerosol sample layer respectively. Blue shading represents the location of the CCNR activation chamber and red shading represents the location of the CCNS activation chamber.

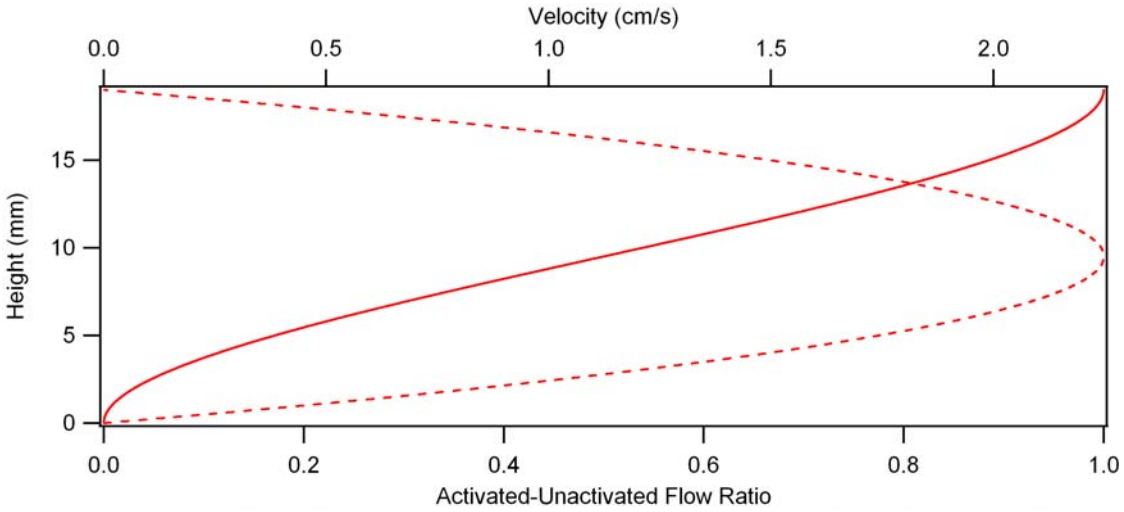

Figure 7. Simulated velocity profile inside the CCNS for S=.35 (dashed curve) with the vertical flow cutoff position in the exit region (solid line) based on the activated to unactivated flow ratio.

3. INSTRUMENT PERFORMANCE

Calibration data measured from the DS_cS for S_c ranges of 0.15%-0.175%, 0.30%-0.35%, and 0.60%-0.70% are shown in Figure 8. In each case, polydisperse ammonium sulfate calibration aerosol was generated using a TSI 3075 constant output atomizer, dried, charged and injected into the sample inlet of the DS_cS. Aerosol size distributions were measured downstream with a scanning DMA system (Wang and Flagan, 1989). Diameters at the half height of the calibration distributions are used with Köhler Theory to determine the actual S_c range separated by the DS_cS, the average of which is defined as $\overline{S_c^*}$. Calculations of instrument resolution, defined to be critical supersaturation at peak $dN/d\log D_p$ (S_c^*) divided by the width of calculated critical supersaturation at the half height of a calibration distribution, are used to quantify performance of the DS_cS between different measurement ranges. Both the slope of the calibration distribution and the supersaturation range used influence the resolution value with more emphasis on the former due to a higher dependence on instrument separation efficiency. Consistency in resolution, hence, stability between the different S_c measurement ranges is illustrated in Figure 9 by normalizing the data on both axes. The three plots presented each have a theoretical perfect resolution of 6.5, defined as the resolution obtained if the calibration distribution half heights are perfectly aligned at diameters corresponding to the prescribed S_c range and the S_c^* value is equal $\overline{S_c^*}$. The calibration data shown have resolution values of 3.84 (0.15-0.175%), 4.11 (0.30-0.35%), and 3.84 (0.60-0.70%), all over half of the theoretical perfect value. Resolution values within this range are

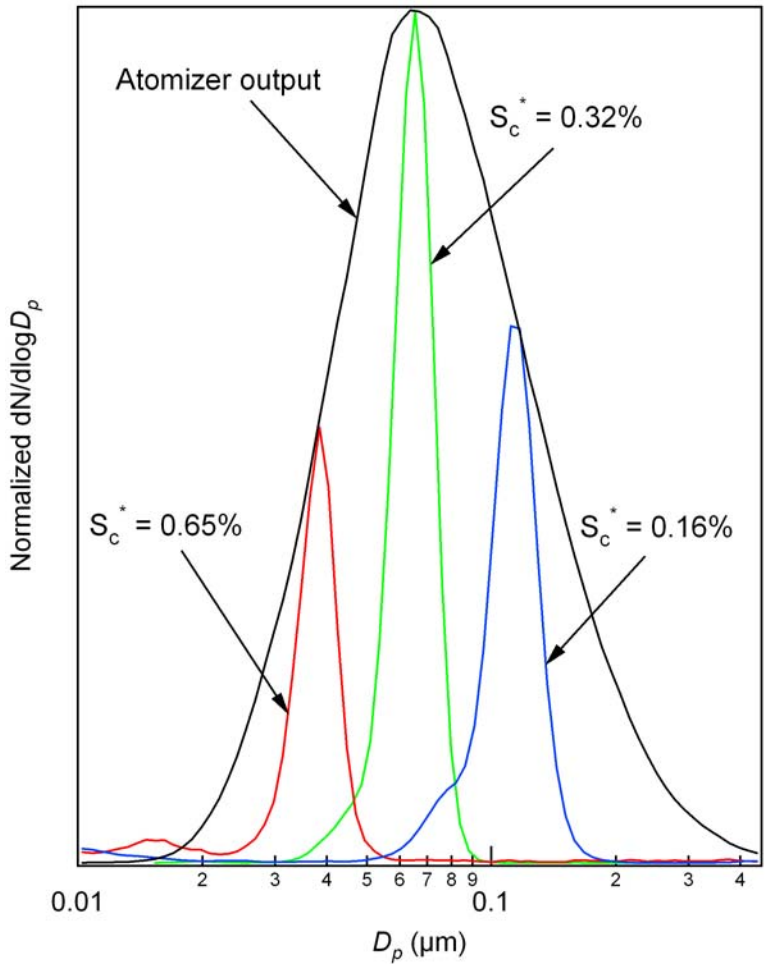

Figure 8. Example activated calibration aerosol distributions at different supersaturation ranges. Theoretical critical supersaturations at peak $dN/dlogD_p$ (S_c^*) are denoted. Data are fitted beneath a sample polydisperse ammonium sulfate atomizer size distribution. Note the minimal overlap from distribution to distribution, illustrating distinct separation ranges of the instrument.

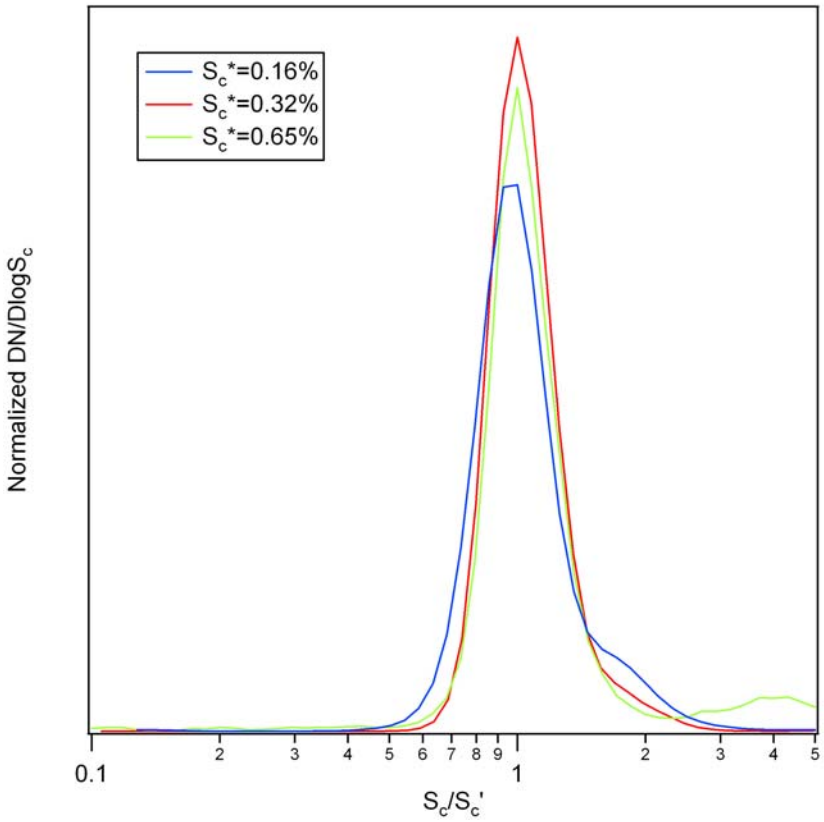

Figure 9. Measured calibration distributions at three supersaturation ranges normalized on both axes. S_c* denotes the calculated critical supersaturation at the peak of the measured distribution.

considered to be within acceptable limits since aerosol properties within the measured supersaturation ranges are discernable as illustrated by ample separation between the different calibration size distributions (Figure 8)

Degradation of DS_cS resolution stems from disturbances in air flow, water flow, and or water temperature. At low S_c values, flow rates are slow resulting in less pressure drop through the inlet tubes, producing a broader layer of sample aerosol closer to the walls of the chamber. This added thickness may expose particles to a broader S range in the chamber, decreasing resolution. Irregular water circulations at the surface of the lower baths also lower resolution, since irregular air flow circulations can develop above the water disturbances. Small differences in temperature throughout the chamber can also cause decreased resolution resulting from deviations in the peak supersaturation. For example, in the temperature ranges the DS_cS is operated at, a temperature anomaly of 0.5ºC translates roughly to a 0.10% change in supersaturation. However, rapid water turnover rates are expected to subdue this effect. As tested, the operational supersaturation range of the DS_cS is between 0.15 to 0.70% and is constrained by the above effects on resolution. To operate outside of this range would introduce the risk of lowered resolution.

Temporal operational stability is of similar importance to instrument resolution since is can influence resolution values. As illustrated in Figure 10, the ability for the DS_cS to consistently maintain set point flow rates and temperatures permit long stable sampling periods. Concerns of degraded water/solution purity over time are addressed by replacing bath fluids on a weekly basis.

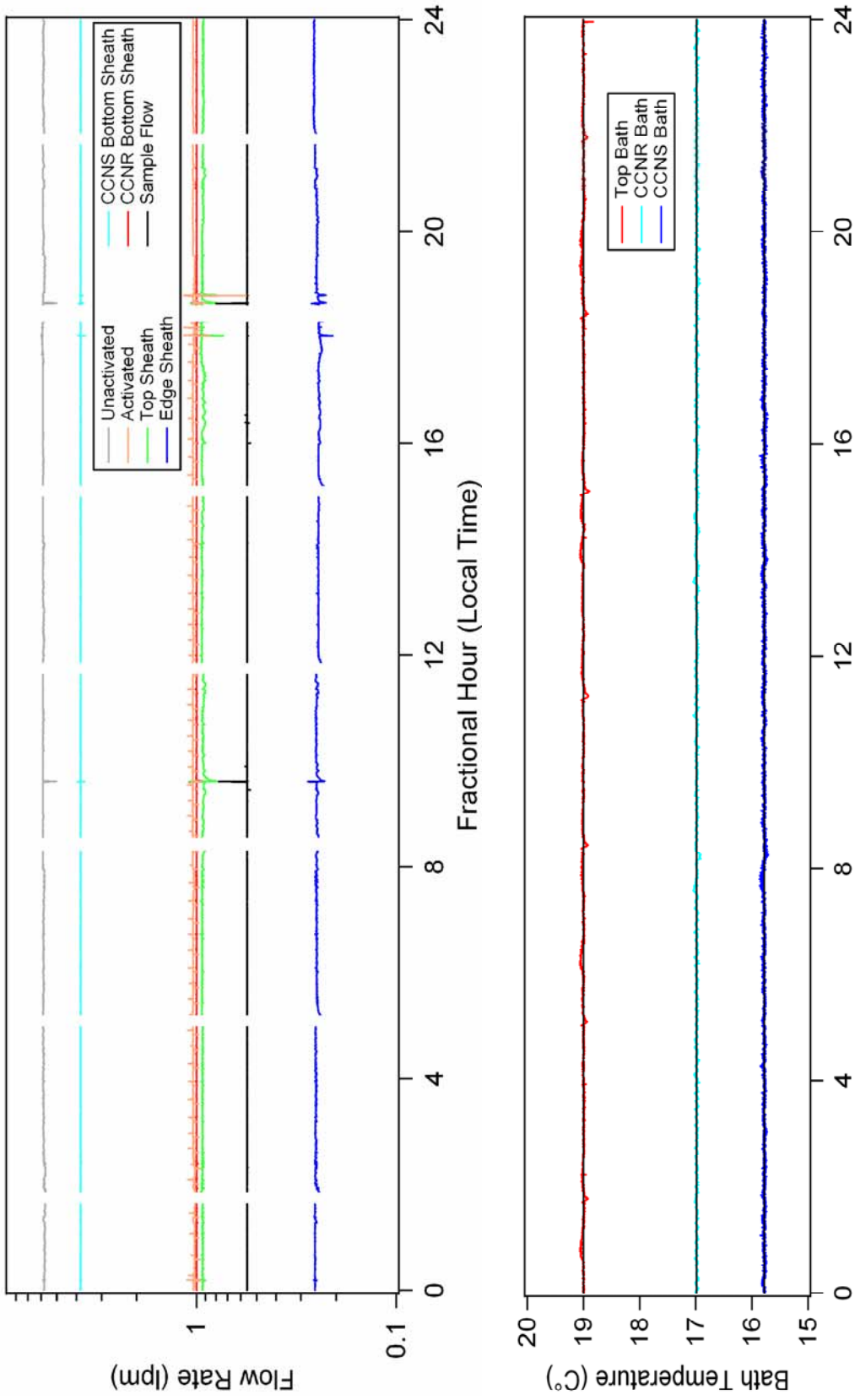

Figure 10. Measured DS_cS temperatures and flow rates. The horizontal black lines indicate individual bath set point temperatures.

4. FIELD DATA

The DS_cS was deployed for the March 2006 MIRAGE field campaign during which size distributions and size-resolved growth factor distributions of ambient aerosol, previously activated in the DS_cS with $\overline{S_c}$ * values ranging between 0.135-0.190%, were measured downstream with a Differential Mobility Analyzer/Tandem Differential Mobility Analyzer (DMA/TDMA) system. Explanations of size-distribution retrieval, size-resolved growth factor distribution retrieval, and operational configuration of the DMA/TDMA system are described in the work of Gasparini et al. (2006). All size-resolved growth factor measurements, defined to be the diameter of a hydrated particle at a reference relative humidity (RH) divided by the initial dry diameter (D_p*) of the same particle, were taken at a constant RH set point of 85% and will be referred to as G(85). Measurement sequences in the DMA/TDMA system last about 30 minutes and consist of a size distribution scan followed by a sequence of size-resolved growth factor measurements taken at predetermined D_p* values. Size distributions of DS_cS separated aerosols were typically observed within the size range of 0.08-0.20 μm, therefore, 0.10, 0.15, and 0.20 μm were used for D_p* in the G(85) distributions. Calibrations of the DS_cS were performed, as described in the calibration section, with ammonium sulfate calibration aerosol throughout the campaign to determine the S_c range separated and ensure proper instrument operation.

4.1 Inversion/Analysis Method

All data were initially analyzed using a Twomey based inversion algorithm (Collins et al., 2002). Ambient aerosol growth factor distributions generally do not change rapidly with respect to D_p*, minimizing influences from multiply charged particles in the distributions. However, this cannot be ignored when considering aerosols separated in the DS_cS due to observed drastic changes in hygroscopicity with respect to D_p*. Consequently, a modification to the inversion algorithm was made to quantify multiply charged particles in the G(85) distributions. Following the initial inversion process, all inverted G(85) distributions were parameterized using lognormal fits. This process involves first determining a number of lognormal modes that combine to represent the entire G(85) distribution. Number concentrations and standard deviations of these lognormal modes are subsequently varied until the mean square error obtained when comparing the distribution that is to be fitted to the resulting parameterized distribution is minimized.

4.2 Observations and Discussion

Figure 11 shows time series plots of ambient size distributions, DS_cS size distributions, and DS_cS 0.15 μm G(85) distributions from March 29-30 which are representative of the MIRAGE field campaign. All data presented in Figure 11 are normalized to clearly depict relative locations of measured size and G(85) distributions. Observed temporal variations in the DS_cS separation size range prove to be minimal when compared to temporal variations in the ambient aerosol size distributions,

indicating no correlation between the two. Temporal variations in the G(85) distributions seem to have a greater dependence on the position of the DS_cS separation range than on the shape of the ambient size distribution. This is apparent in data collected between the fractional day (FD) of 29.55 and 29.70 where a slight decrease in diameters of the separation size range corresponds to decreased hygroscopicity at 0.15 µm. The shift in the separated size range to smaller diameters indicates that the aerosol population is more efficient at activation which could result from aerosol with an increased fraction of solute, or the presence of a surface tension reducing chemical compound. Figure 12 shows ambient size distributions measured before and during this time period with lognormal fits to the distributions indicated. A shift in the parameterized modes is observed when considering their fractional contributions to the concentration at 0.15 µm at both times, which corresponds to the diameter shift in the DS_cS separation range. The shift in ambient aerosol combined with decreased hygroscopicity at 0.15 µm further suggests the presence/addition of a surface tension reducing organic with limited hygroscopicity and/or a solute with limited solubility at 85% RH.

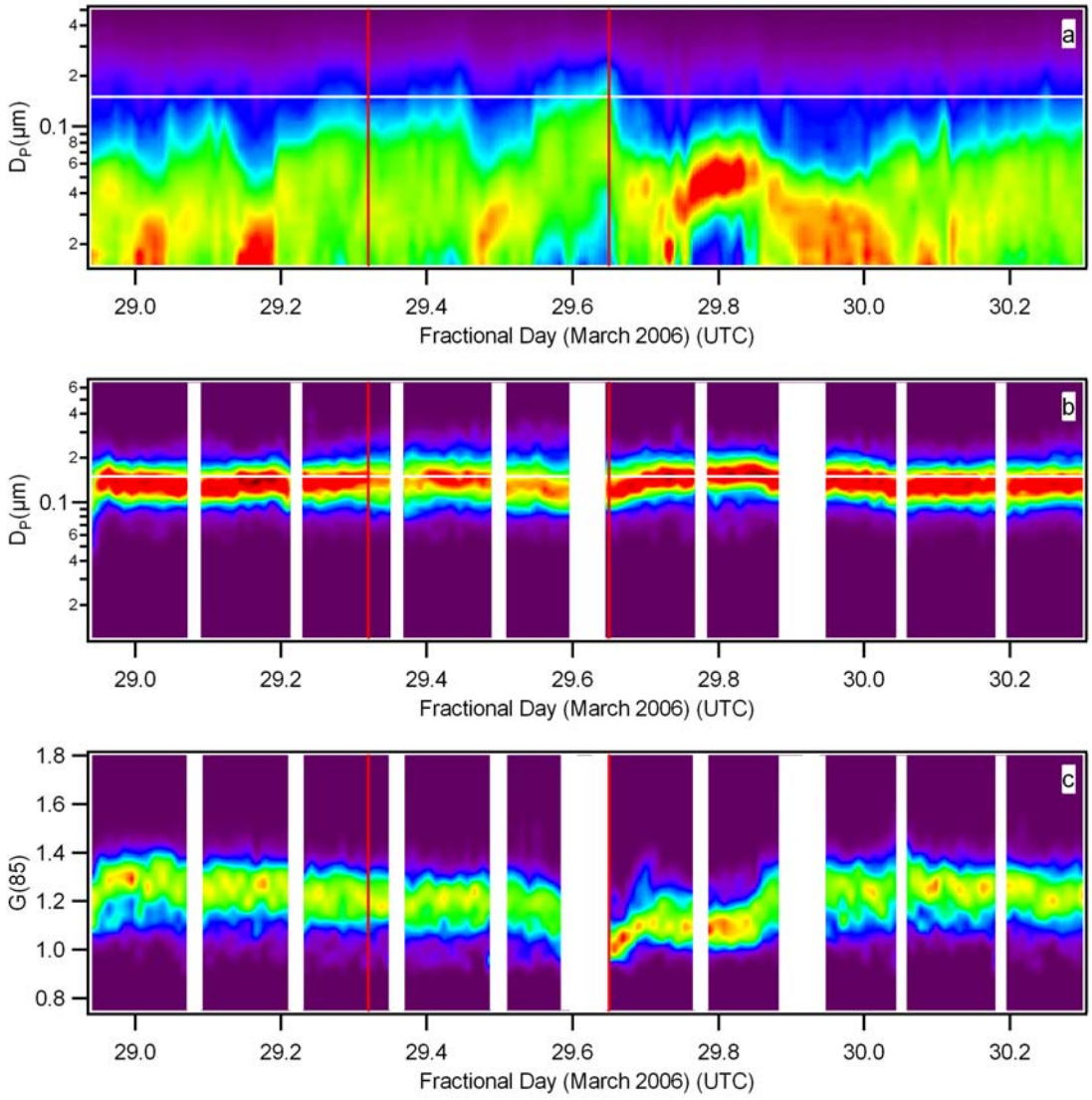

Figure 11. Normalized temporal plots of a.) ambient size distributions, b.) ambient DScS separated size distributions, and c.) G(85) distributions at 0.15 µm. Horizontal white lines on Figures a and b represent the location of 0.15 µm. Vertical red lines represent location of data presented in Figure 12. Breaks in data, indicated with white vertical stripes, occurred as a result of instrument calibration and during periodic soak cycles.

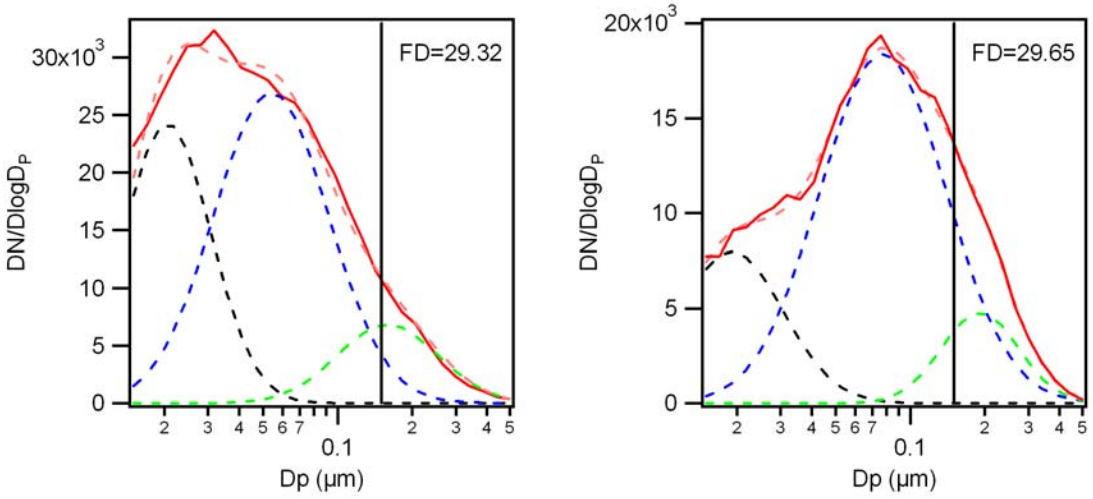

Figure 12. Parameterized ambient size distributions at the fractional days (FD) noted. Vertical black lines indicate the location of 0.15 µm. Individual parameterized modes are represented by colored dashed lines, the sums of which are represented by the red dashed line. Note the shift in the dominant mode at 0.15 µm between the two plots.

Unlike aerosols measured in the time frame discussed above, measurements taken between FD 29.70 and 29.90 show a shift to relatively larger diameters separated in the DS_cS. Ambient size distributions at the same time evolve to a larger mean size perhaps as a result of an increase in the internally mixed organic fraction of the aerosol due to condensation/sorption reactions. Growth factor measurements support this claim since values are centered around 1.1 (Cruz and Pandis, 2000; Cocker et al., 2001; Baltensperger et al., 2005; Varutbangkul et al., 2006). Outside of these two time ranges, G(85) measurements follow a consistent trend, ranging between 1.175 and 1.350. It is important to note that although there seems to be a dependence between DS_cS separation size range location and G(85) measurements, a clear relationship between S_c and hygroscopicity is not evident. A method developed to determine such a relationship is described below.

Following G(85) distribution parameterization, patterns were observed showing that with the exception of a small fraction of measurements, ancillary modes contribute less than 22% to the total concentration. Thus, dominant hygroscopic features are isolated when considering only primary modes in the parameterized data. However, data are omitted when it is apparent that the algorithm implemented in the data inversion

process does not effectively account for multiply charged particles in the G(85) distributions. Inaccurate predictions of the aforementioned particles stem from variability of ambient aerosol properties over scan times of approximately 30 minutes and from uncertainties in the charging probability of ambient aerosol. Figure 13 shows histograms, generated for different time periods, of median values in the primary G(85) modes at the D_p* values measured. Abrupt changes in G(85) with respect to D_p* are evident in all histograms with larger D_p* values corresponding to smaller G(85) values. At 0.20 µm, G(85) measurements rarely exceed 1.15 with all histogram peaks located at values less than 1.10 excluding the peak just exceeding 1.10 on Mar 17-18. As described above, the limited hygroscopicity of theses particles suggests a chemical composition composed of mainly carbonaceous compounds. G(85) values at 0.15 and 0.10 µm are more variable perhaps as a result from higher sensitivity to small shifts in the S_c separation range and/or higher sensitivity to ambient aerosol chemical composition.

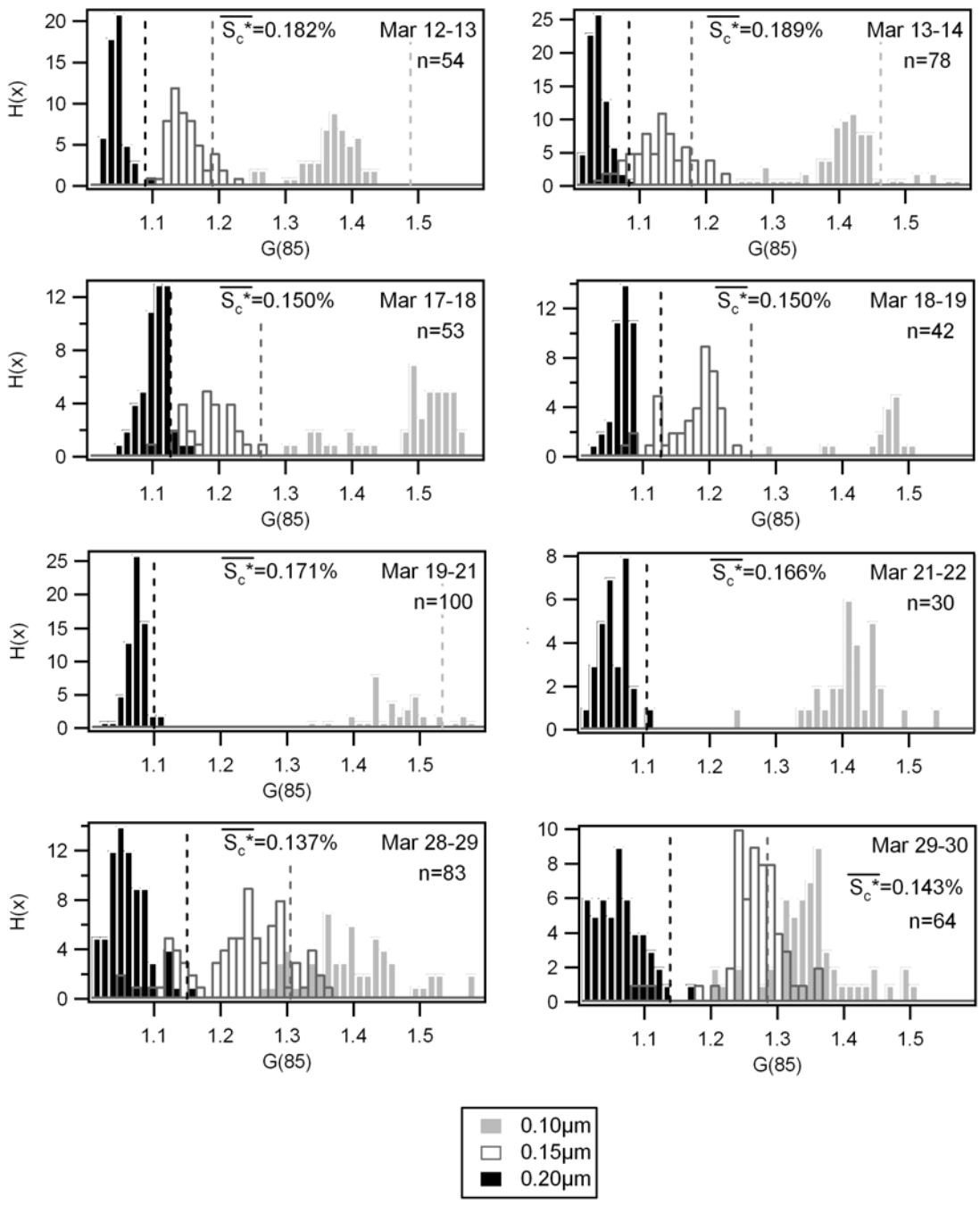

Figure 13. Histograms of primary parameterized G(85) mode median values at indicated sizes throughout MIRAGE. Time periods in each figure are segregated by inconsistent DS_cS operation periods. Vertical dashed lines represent values of predicted growth factors. The number of measurement sequences used in each plot is denoted by n.

Predictions of G(85) values for particles in thermodynamic equilibrium are performed using modified Köhler Theory where S, as described by Seinfeld and Pandis, (1998), takes the form:

$$\frac{e'}{e_s} = \gamma_w \chi_w \exp\left[\frac{4M_w\sigma_{as}}{RT\rho_w D_d}\right] \tag{7}$$

In the equation above, e' and e_s are the vapor pressure adjacent to a droplet surface and the saturation vapor pressure, respectively, M_w and ρ_w denote the molecular weight and density of water, respectively, σ_{as} is the surface tension of aqueous solution, T is temperature, D_d is droplet diameter, and χ_w and γ_w represent the mole fraction of water in solution and activity coefficient, respectively. At RH values greater than 100%, a droplet is assumed to behave ideally by which γ_w approaches the value of 1 and χ_w can be written as:

$$\chi_w = \frac{1}{\frac{iM_w}{M_s}\left(\frac{\varepsilon_s}{1-\varepsilon_s}\right)+1} \tag{8}$$

where ε_s is the mass fraction of solute in aqueous solution, M_s is the molecular weight of soluble material, and i is the number of dissociated ions in solution per molecule (van't Hoff factor). To determine ε_s the empirical relationships described by Tang and Munkelwitz, 1994 are used in the following equations for ρ_{as} (density of aqueous solution) and α_w (water activity):

$$\frac{m_s}{\varepsilon_s\rho_{as}} - \frac{m_s}{\rho_s} = \frac{\pi}{6}\left(D_{p(RH)}^3 - D_p^{*3}\right) \tag{9}$$

$$RH = \alpha_w \exp\left[\frac{4M_w\sigma_{as}}{RT\rho_w(G(RH)*D_p^*)}\right] \quad (10)$$

Where RH=0.85 and m_s and ρ_s are the mass and density of soluble material, respectively. In equations (7) and (10) σ_{as} is represented by:

$$\sigma_{as} = \sigma_w(T) + \frac{2\times10^{-6}\varepsilon_s\rho_{as}}{M_s} \quad (11)$$

If the solution is assumed to behave ideally in subsaturated conditions, the empirical relationship describing ρ_{as} becomes:

$$\rho_{as} = \frac{1}{\left(\frac{1-\varepsilon_s}{\rho_w}\right)+\frac{\varepsilon_s}{\rho_s}} \quad (12)$$

and α_w takes the form of χ_w in equation (8). Iterations of equations (9) and (10) are taken at 298K, the temperature inside of the TDMA, by varying ε_s until both conditions are satisfied. The soluble mass of the particle is then determined from equation (9) and held fixed in the ε_s term. Once soluble mass is determined, iterations of equation (7) are taken by varying ε_s until $dS/d\varepsilon_s = 0$, yielding S_c. This process is repeated with various G(85) values at 291K, the temperature inside of the DS_cS, until $S_c = \overline{S_c^*}$.

A study on chemical characterization of Mexico City ambient aerosol indicates that during the month of April 2003 the primary inorganic chemical constituents were ammonium sulfate and ammonium nitrate (Salcedo et al., 2006). Contributions of these substances represented, on average, about 10% each to the total ambient aerosol mass,

whereas organics accounted for just over half the total mass. Organics, represented by hundreds of different chemical compounds possessing different activation properties, are assumed to be insoluble, while all soluble material in equations (7-12) is assumed to be composed of inorganics. Furthermore, since minimal information describing activation efficiency of ammonium nitrate is available, all calculations in this section assume aerosols composed of an insoluble core surrounded by an ammonium sulfate shell. Either a van't Hoff factor of 2.3 or an empirical equation that determines van't Hoff factor from molality is used in equation (8) (Young and Warren, 1992; Svenningsson et al., 2006).

Dashed vertical lines in Figure 13 represent calculated growth factors for all D_p* values using empirical fits for subsaturated conditions and assuming i=2.3. Growth factor calculations that exceed the maximum growth factor possible for ammonium sulfate at a respective size are not shown. If the ambient aerosols activate according to predictions, the dashed vertical lines should lie roughly at the midpoint of their corresponding histogram. Instead, however, most of the calculated G(85) values are skewed towards larger growth factors.

A matrix of S_c values calculated using equation (7) with several D_p* and G(85) combinations yields contours of constant S_c illustrated in Figure 14. Increased sensitivity of S_c at small growth factors is apparent when considering spacing between the contours. Mean G(85) values of dominant parameterized modes throughout MIRAGE are included as well, with whiskers representing one standard deviation in the data. Lines of similar color represent extents of the S_c separation range, the mean value

of which equals $\overline{S_c}^*$, determined from calibration data. Although a few mean G(85) values lie close to corresponding $\overline{S_c}^*$ values (labeled in Figure 13), most do not. Plausible explanations for this discrepancy ensue from uncertainties in the assumptions used in equations (7-12). Figures 13 and 14 suggest that S_c values in Mexico City should be larger than observed. Acknowledging a consistent presence of a surface tension reducing organic compound and/or solute with limited solubility would serve to reduce calculated S_c values throughout the project.

Estimated correction factors applied to S_c derived using hygroscopicity for the measurement conditions described above are given in table 1, which shows mean ratios of derived S_c values at observed mean G(85) values to $\overline{S_c}^*$ using the empirical, ideal, and variable van't Hoff factor Köhler Theory calculations. The enlargement of this ratio at 0.2 μm suggests that aerosols with larger organic fractions produce the largest discrepancy in calculated to predicted S_c. Smaller ratios at the remaining two size classes correspond to aerosol with larger inorganic fractions.

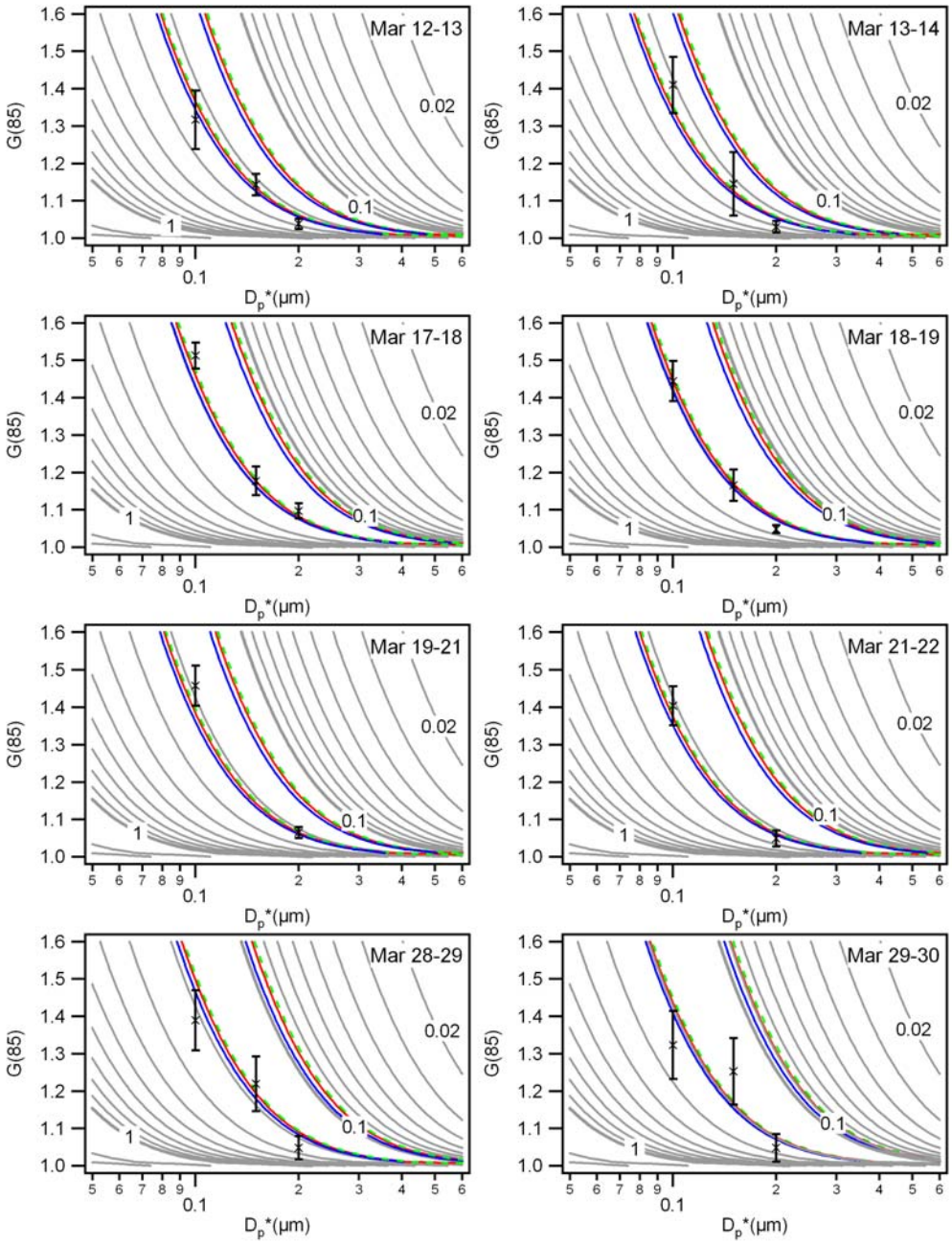

Figure 14. Simulated contours of constant S_C, calculated assuming an ammonium sulfate inorganic fraction, for the same time intervals used in Figure 13. Grey curves represent calculations assuming a non-ideal solution in subsaturated conditions. Red curves represent boundaries of the separation range in the DScS using the above assumptions (empirical calculations). Green dashed curves represent the same boundaries calculated assuming an ideal solution in subsaturated conditions (ideal calculations). Blue curves represent the same boundaries calculated using the empirical calculations and a variable van't Hoff factor. X denotes the mean value of parameterized G(85) data and is centered within one standard deviation whiskers.

Table 1. Average ratios of calculated S_c to measured S_c for all three calculation assumptions.

D_p* (μm)	Ideal Solution	Empirical Fits	Variable van't Hoff factor
0.10	1.318	1.290	1.235
0.15	1.228	1.199	1.145
0.20	1.533	1.496	1.440

5. CONCLUSION

The measurement of CCN isolated from unactivated aerosol provides a more direct link between CCN concentrations and aerosol properties, however, few instruments have been designed to perform this task. A lack in the development of this type of CCN instrumentation has prompted the development of a new novel instrument named the DS_cS. The design of the DS_cS incorporates two continuous flow parallel plate thermal gradient diffusion cloud chambers into one continuous chamber that first removes CCN at a pre-determined S_c and subsequently isolates CCN in the remaining sample aerosol at a second pre-determined S_c. This unique orientation of cloud activation chambers facilitates not only the isolation of CCN from unactivated aerosol, it also constrains the supersaturation range sample aerosol activate within and allows separate instrumentation to sample both activated and unactivated aerosols downstream.

An intricate system of water and air flow control through the DS_cS chamber provides days of continuous operation following a stabilization time of 2-3 hours. To test instrument operational theory, polydisperse ammonium sulfate aerosol were injected into the DS_cS and sampled downstream with a scanning DMA system. The unique size dependence of calibration aerosol to S_c should and does produce a narrow size distribution that resembles a monodisperse aerosol population. Resolution values, defined as the S_c at peak $dN/d\log D_p$ of the calibration size distribution divided by the full width of S_c at its half height, are obtained from calibration data and are over half of the theoretical perfect resolution values indicating sharp S_c separation in both activation

chambers. The tested operation S_c range is between 0.15% and 0.7%, separation outside of this range introduces a risk of lowered resolution.

Size distributions and hygroscopic growth factor distributions of DS_cS classified aerosols, measured during the March 2006 MIRAGE field campaign, were analyzed to study urban aerosol CCN activation properties in Mexico City, Mexico. Growth factor predictions of aerosols with known S_c, calculated using a modified version of Köhler Theory, are compared to measured mean growth factors at the same S_c throughout the campaign. Results show predicted growth factors of DS_cS separated aerosol are often larger than measured values. This observation is indicative of aerosols that are more efficient at activation than theory suggests. Interestingly enough, closure studies often report an over prediction of anthropogenically influenced CCN, hinting that urban aerosols are often less efficient at activation than theory suggests (Chuang et al., 2000; Cantrell et al., 2001). Whether this is a localized effect or typical of other environments is not discernable from this study. Hence, more research needs to be conducted to ascertain the source of this discrepancy.

Development of the DS_cS has opened the doors to a different type of CCN analysis. The ability to focus measurements of previously activated aerosols between a narrow supersaturation range permits downstream analysis of CCN at the threshold of activation. Examining CCN at this threshold allows for a more detailed analysis of activation properties, leading to higher accuracy in predictions of particle activation efficiency.

REFERENCES

Ackerman, A. S., Toon, O. B., Taylor, J. P., Johnson, D. W., Hobbs, P. V. and Ferek, R. J. (2000). Effects of aerosols on cloud albedo: Evaluation of Twomey's parameterization of cloud susceptibility using measurements of ship tracks, *J. Atmos. Sci.* 57(16):2684-2695.

Adams, P. J. and Seinfeld, J. H. (2002). Predicting global aerosol size distributions in general circulation models, *J. Geophys. Res.-Atmos.* 107(D19):4370 doi:10.1029/2001JD001010.

Adams, P. J. and Seinfeld, J. H. (2003). Disproportionate impact of particulate emissions on global cloud condensation nuclei concentrations, *Geophys. Res. Lett.* 30(5):1239 doi:10.1029/2002GL016303.

Aitken, J. (1880a). On dust, fogs and clouds, *Proc. R. Soc.* 11:14-18.

Aitken, J. (1880b). On dust, fogs and clouds, *Nature* Feb.:384-385.

Alofs, D. J. (1978). Performance of a dual-range cloud nucleus counter, *J. Appl. Meteorol.* 17(9):1286-1297.

Alofs, D. J., Williams, A. L., Hagen, D. E., Medley, S. D., White, D. R. and Schmitt, J. (1997). A system for collecting milligram quantities of cloud condensation nuclei, *Aerosol Sci. Tech.* 26(5):415-432.

Baltensperger, U., Kalberer, M., Dommen, J., Paulsen, D., Alfarra, M. R., Coe, H., Fisseha, R., Gascho, A., Gysel, M., Nyeki, S., Sax, M., Steinbacher, M., Prevot, A.

S. H., Sjoren, S., Weingartner, E. and Zenobi, R. (2005). Secondary organic aerosols from anthropogenic and biogenic precursors, *Faraday Discuss.* 130:265-278.

Bilde, M. and Svenningsson, B. (2004). CCN activation of slightly soluble organics: the importance of small amounts of inorganic salt and particle phase, *Tellus B* 56(2):128-134.

Cantrell, W., Shaw, G., Cass, G. R., Chowdhury, Z., Hughes, L. S., Prather, K. A., Guazzotti, S. A. and Coffee, K. R. (2001). Closure between aerosol particles and cloud condensation nuclei at Kaashidhoo Climate Observatory, *J. Geophys. Res.-Atmos.* 106(D22):28711-28718.

Charlson, R. J., Schwartz, S. E., Hales, J. M., Cess, R. D., Coakley, J. A., Hansen, J. E. and Hofmann, D. J. (1992). Climate forcing by anthropogenic aerosols, *Science* 255(5043):423-430.

Chuang, P. Y., Collins, D. R., Pawlowska, H., Snider, J. R., Jonsson, H. H., Brenguier, J. L., Flagan, R. C. and Seinfeld, J. H. (2000). CCN measurements during ACE-2 and their relationship to cloud microphysical properties, *Tellus B* 52(2):843-867.

Cocker, D. R., Mader, B. T., Kalberer, M., Flagan, R. C. and Seinfeld, J. H. (2001). The effect of water on gas-particle partitioning of secondary organic aerosol: II. m-xylene and 1,3,5-trimethylbenzene photooxidation systems, *Atmos. Environ.* 35:6073-6085.

Collins, D. R., Flagan, R. C. and Seinfeld, J. H. (2002). Improved inversion of scanning DMA data, *Aerosol Sci. Tech.* 36(1):1-9.

Covert, D. S., Gras, J. L., Wiedensohler, A. and Stratmann, F. (1998). Comparison of directly measured CCN with CCN modeled from the number-size distribution in the

marine boundary layer during ACE 1 at Cape Grim, Tasmania, *J. Geophys. Res.-Atmos.* 103(D13):16597-16608.

Cruz, C. N. and Pandis, S. N. (2000). Deliquescence and hygroscopic growth of mixed inorganic-organic atmospheric aerosol, *Environmental Science & Technology* 34(20):4313-4319.

Fukuta, N. and Walter, L. A. (1970). Kinetics of hydrometeor growth from a vapor-spherical model, *J. Atmos. Sci.* 27(8):1160-1172.

Gasparini, R., Collins, D. R., Andrews, E., Sheridan, P. J., Ogren, J. A. and Hudson, J. G. (2006). Coupling aerosol size distributions and size-resolved hygroscopicity to predict humidity-dependent optical properties and cloud condensation nuclei spectra, *J. Geophys. Res.-Atmos.* 111(D5S13): doi:10.1029/2005JD006092.

Glantz, P., Noone, K. J. and Osborne, S. R. (2003). Comparisons of airborne CVI and FSSP measurements of cloud droplet number concentrations in marine stratocumulus clouds, *J. Atmos. Ocean. Tech.* 20(1):133-142.

Gong, S. L., Barrie, L. A. and Blanchet, J. P. (1997). Modeling sea-salt aerosols in the atmosphere .1. Model development, *J. Geophys. Res.-Atmos.* 102(D3):3805-3818.

Harrison, L. and Harrison, H. (1985). The segregation of aerosols by cloud-nucleating activity. Part 1: Design, construction, and testing of a high-flux thermal-diffusion cloud chamber for mass separation, *J. Clim. Appl. Meteorol.* 24(4):302-310.

Hegg, D. A., Covert, D. S., Jonsson, H., Khelif, D. and Friehe, C. A. (2004). Observations of the impact of cloud processing on aerosol light-scattering efficiency, *Tellus B* 56(3):285-293.

Henning, S., Rosenorn, T., D'Anna, B., Gola, A. A., Svenningsson, B. and Bilde, M. (2005). Cloud droplet activation and surface tension of mixtures of slightly soluble organics and inorganic salt, *Atmos. Chem. Phys. Discuss.* 5:575-582.

Ji, Q., Shaw, G. E. and Cantrell, W. (1998). A new instrument for measuring cloud condensation nuclei: Cloud condensation nucleus "remover", *J. Geophys. Res.-Atmos.* 103(D21):28013-28019.

Jones, A., Roberts, D. L., Woodage, M. J. and Johnson, C. E. (2001). Indirect sulphate aerosol forcing in a climate model with an interactive sulphur cycle, *J. Geophys. Res.-Atmos.* 106(D17):20293-20310.

Noone, K. J., Ogren, J. A., Heintzenberg, J., Charlson, R. J. and Covert, D. S. (1988). Design and calibration of a counterflow virtual impactor for sampling of atmospheric fog and cloud droplets, *Aerosol Sci. Tech.* 8(3):235-244.

Ogren, J. A., Heintzenberg, J. and Charlson, R. J. (1985). Insitu sampling of clouds with a droplet to aerosol converter, *Geophys. Res. Lett.* 12(3):121-124.

Penner, J. E., Hegg, D. and Leaitch, R. (2001). Unraveling the role of aerosols in climate change, *Environ. Sci. Technol.* 35(15):332a-340a.

Pruppacher, H. R. and Klett, J. D. (1978). Microphysics of clouds and precipitation. D. Reidel Pub. Co., Dordrecht, Holland.

Roberts, G. C. and Nenes, A. (2005). A continuous-flow streamwise thermal-gradient CCN chamber for atmospheric measurements, *Aerosol Sci. Tech.* 39(3):206-221.

Rosenfeld, D. (1999). TRMM observed first direct evidence of smoke from forest fires inhibiting rainfall, *Geophys. Res. Lett.* 26(20):3105-3108.

Salcedo, D., Onasch, T. B., Dzepina, K., Canagaratna, M. R., Zhang, Q., Huffman, J. A., DeCarlo, P. F., Jayne, J. T., Mortimer, P., Worsnop, D. R., Kolb, C. E., Johnson, K. S., Zuberi, B., Marr, L. C., Volkamer, R., Molina, L. T., Molina, M. J., Cardenas, B., Bernabe, R. M., Marquez, C., Gaffney, J. S., Marley, N. A., Laskin, A., Shutthanandan, V., Xie, Y., Brune, W., Lesher, R., Shirley, T. and Jimenez, J. L. (2006). Characterization of ambient aerosols in Mexico City during the MCMA-2003 campaign with Aerosol Mass Spectrometry: results from the CENICA Supersite, *Atmos. Chem. Phys.* 6:925-946.

Seinfeld, J. H. and Pandis, S. N. (1998). Atmospheric chemistry and physics: from air pollution to climate change. John Wiley & Sons, Inc., New York.

Shaw, R. A. and Lamb, D. (1999). Experimental determination of the thermal accommodation and condensation coefficients of water, *J. Chem. Phys.* 111(23):10659-10663.

Sinnarwalla, A. M. and Alofs, D. J. (1973). A cloud nucleus counter with long available growth time, *J. Appl. Meteorol.* 12:831-835.

Sorooshian, A., Varutbangkul, V., Brechtel, F. J., Ervens, B., Feingold, G., Bahreini, R., Murphy, S. M., Holloway, J. S., Atlas, E. L., Buzorius, G., Jonsson, H., Flagan, R. C. and Seinfeld, J. H. (2006). Oxalic acid in clear and cloudy atmospheres: Analysis of data from International Consortium for Atmospheric Research on Transport and Transformation 2004, *J. Geophys. Res.-Atmos.* 111(D23S45): doi:10.1029/2005JD006880.

Spracklen, D. V., Pringle, K. J., Carslaw, K. S., Chipperfield, M. P. and Mann, G. W. (2005). A global off-line model of size-resolved aerosol microphysics: I. Model development and prediction of aerosol properties, *Atmos. Chem. Phys. Discuss.* 5:179-215.

Sun, L. K. and Reiss, H. (1984). Measurement of the properties of single aerosol drops using a new means of suspension, *J. Colloid Interf. Sci.* 99(2):515-535.

Svenningsson, B., Rissler, J., Swietlicki, E., Mircea, M., Blide, M., Facchini, M. C., Decesari, S., Fuzzi, S., Zhou, J., Mønster, J. and Rosenørn, T. (2006). Hygroscopic growth and critical supersaturations for mixed aerosol particles of inorganic and organic compounds of atmospheric relevance, *Atmos. Chem. Phys.* 6(1937-1952.

Tang, I. N. and Munkelwitz, H. R. (1994). Water activities, densities, and refractive-indexes of aqueous sulfates and sodium-nitrate droplets of atmospheric importance, *J. Geophys. Res.-Atmos.* 99(D9):18801-18808.

Twohy, C. H., Hudson, J. G., Yum, S. S., Anderson, J. R., Durlak, S. K. and Baumgardner, D. (2001). Characteristics of cloud-nucleating aerosols in the Indian Ocean region, *J. Geophys. Res.-Atmos.* 106(D22):28699-28710.

Twomey, S. (1963). Measurements of natural cloud nuclei, *J. Rech. Atmos.* 1(101-105.

Twomey, S. (1977). Influence of pollution on shortwave albedo of clouds, *J. Atmos. Sci.* 34(7):1149-1152.

VanReken, T. M., Ng, N. L., Flagan, R. C. and Seinfeld, J. H. (2005). Cloud condensation nucleus activation properties of biogenic secondary organic aerosol, *J. Geophys. Res.-Atmos.* 110(D07206): doi:10.1029/2004JD005465.

VanReken, T. M., Rissman, T. A., Roberts, G. C., Varutbangkul, V., Jonsson, H. H., Flagan, R. C. and Seinfeld, J. H. (2003). Toward aerosol/cloud condensation nuclei (CCN) closure during CRYSTAL-FACE, *J. Geophys. Res.-Atmos.* 108(D20):4633 doi:10.1029/2003JD003582.

Varutbangkul, V., Brechtel, F. J., Bahreini, R., Ng, N. L., Keywood, M. D., Kroll, J. H., Flagan, R. C., Seinfeld, J. H., Lee, A. and Goldstein, A. H. (2006). Hygroscopicity of secondary organic aerosols formed by oxidation of cycloalkenes, monoterpenes, sesquiterpenes, and related compounds, *Atmos. Chem. Phys.* 6:2367-2388.

Wang, S. C. and Flagan, R. C. (1989). Scanning electrical mobility spectrometer, *J. Aerosol Sci.* 20(8):1485-1488.

Wobrock, W., Flossmann, A. I., Monier, M., Pichon, J. M., Cortez, L., Fournol, J. F., Schwarzenbock, A., Mertes, S., Heintzenberg, J., Laj, P., Orsi, G., Ricci, L., Fuzzi, S., Ten Brink, H., Jongejan, P. and Otjes, R. (2001). The Cloud Ice Mountain Experiment (CIME) 1998: Experiment overview and modelling of the microphysical processes during the seeding by isentropic gas expansion, *Atmos. Res.* 58(4):231-265.

Young, K. C. and Warren, A. J. (1992). A reexamination of the derivation of the equilibrium supersaturation curve for soluble particles, *J. Atmos. Sci.* 49(13):1138-1143.

VITA

Name: Robert John Osborn

Address: Department of Atmospheric Sciences, Texas A&M University 3150 TAMU, College Station, TX 77843-3150

Email Address: rjo111@gmail.com

Education: B.S., Meteorology, Texas A&M University, 2002
M.S., Atmospheric Sciences, Texas A&M University, 2007